JACS
JOURNAL OF THE AMERICAN CHEMICAL SOCIETY
Article
pubs.acs.org/JACS

Size-Dependent Morphology of Dealloyed Bimetallic Catalysts: Linking the Nano to the Macro Scale

Mehtap Oezaslan,*[,†] Marc Heggen,[‡] and Peter Strasser[†]

[†]The Electrochemical Energy, Catalysis, and Materials Science Laboratory, Department of Chemistry, Chemical Engineering Division, Technical University Berlin, Sekr. TC03, Strasse des 17. Juni 124, 10623 Berlin, Germany

[‡]Ernst Ruska-Centre for Microscopy and Spectroscopy with Electrons, Forschungszentrum Jülich GmbH, 52425 Jülich, Germany

Supporting Information

ABSTRACT: Chemical dealloying of Pt binary alloy precursors has emerged as a novel and important preparation process for highly active fuel cell catalysts. Dealloying is a selective (electro)chemical leaching of a less noble metal M from a M rich Pt alloy precursor material and has been a familiar subject of macroscale corrosion technology for decades. The atomic processes occurring during the dealloying of nanoscale materials, however, are virtually unexplored and hence poorly understood. Here, we have investigated how the morphology and intraparticle composition depend on the particle size of dealloyed Pt−Co and Pt−Cu alloy nanoparticle precursor catalysts. To examine the size−morphology−composition relation, we used a combination of high-resolution scanning transmission electron microscopy (STEM), transmission electron microscopy (TEM), electron energy loss (EEL) spectroscopy, energy-dispersive X-ray spectroscopy (EDS), and surface-sensitive cycling voltammetry. Our results indicate the existence of three distinctly different size-dependent morphology regimes in dealloyed Pt−Co and Pt−Cu particle ensembles: (i) The arrangement of Pt shell surrounding a single alloy core ("*single core−shell nanoparticles*") is exclusively formed by dealloying of particles below a characteristic diameter $d_{\text{multiple cores}}$ of 10−15 nm. (ii) Above $d_{\text{multiple cores}}$, nonporous bimetallic core−shell particles dominate and show structures with irregular shaped multiple Co/Cu rich cores ("*multiple cores−shell nanoparticles*"). (iii) Above the second characteristic diameter d_{pores} of about 30 nm, the dealloyed Pt−Co and Pt−Cu particles start to show surface pits and nanoscale pores next to multiple Co/Cu rich cores. This structure prevails up to macroscopic bulklike dealloyed particles with diameter of more than 100 nm. The size−morphology−composition relationships link the nano to the macro scale and provide an insight into the existing material gap of dealloyed nanoparticles and highly porous bulklike bimetallic particles in corrosion science.

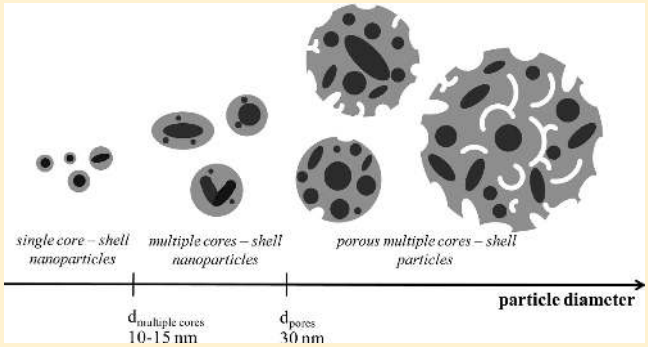

1. INTRODUCTION

Bimetallic alloy nanoparticles are of great importance in diverse areas, such as magnetic, optical and catalytic applications, due to the clearly altered properties compared with monometallic nanoparticles.[1−5] They offer a wide range of compositional (e.g., overall, surface and bulk ratios of metal A and B) and morphological (e.g., particle size, shape and crystal facets) configurations, which sensitively control their surface properties. For instance, dissimilar metals in or near the surface of homogeneously alloyed bimetallic particle catalysts can lead to coexisting surface functionalities and affect the surface reaction kinetics.[6−11]

Core−shell nanoparticles as particular type of arrangement of binary metals have attracted much attention in electrochemical energy conversion.[12−18] They are distinguished by a particle shell of enriched or pure metal A surrounding a core with different composition (pure metal B[19,20] or alloys of metals A and B[21]). Dependent on the shell thickness, the improved surface catalytic reactivity is based on short-range chemical ligand effects and/or long-range geometric effects such as lattice strain.[21−26]

Chemical dealloying has emerged as a novel and important synthesis process to obtain catalytically active core−shell bimetallic particles. Historically, dealloying was used for depletion gilding in ancient societies.[27,28] In 1927 Raney invented the well-known Raney nickel, which is used as a heterogeneous catalyst for hydrogenation reactions.[29] In this century, the selective dissolution of less noble metal from bimetallic alloy system has been mostly studied in the corrosion realm to produce nanoporous materials for catalytic and sensory applications.[30−40] In particular, dealloyed Pt alloy core−shell nanoparticles, formed in situ by the selective surface dissolution of the less noble component from a uniform binary alloy precursor, have shown very promising catalytic reactivities for the electroreduction of dioxygen (oxygen reduction

Received: September 19, 2011
Published: November 30, 2011

 © 2011 American Chemical Society dx.doi.org/10.1021/ja2088162 | J. Am. Chem.Soc. 2012, 134, 514−524

reaction, ORR) to water in polymer electrolyte membrane fuel cells (PEMFCs).[41−45] More precisely, the dealloyed $PtCu_3$ is currently the alloy nanoparticle electrocatalyst which meets and exceeds the cathode catalyst activity targets in RDE experiments and real MEAs for automotive applications.[21,45−50] The significantly improved performance is due to the lattice strain in the Pt rich shell. The strain significantly changes[21] the chemisorption energies of oxygenated reactive intermediates and effects a 4−6 fold activity enhancement of the oxygen reduction.

In our previous work on dealloyed Pt bimetallic alloy fuel cell electrocatalysts, we focused on nanoparticles that exhibited a so-called "single core-shell structure" consisting of a near-concentrical arrangement of a Pt rich shell and a Pt poor alloy rich core. This structure is characterized by a monotone drop of the non noble metal toward the particle surface. We found single core-shell particles of a few nanometers diameter as an important morphological basic type in dealloyed bimetallic nanoparticle ensembles. The morphology and contribution of larger dealloyed particles, however, with their higher intrinsic catalytic activity[51−53] have remained unclear to date. Previous studies have reported on at least one other structural type of bimetallic nanoparticles after acid and/or electrochemical treatment using microscopic and spectroscopic techniques.[54−61] However, until now, no particular emphasis was given how the size of dealloyed bimetallic particles is linked with their intraparticle structure and composition on an atomic scale. A detailed understanding of the size−structure−morphology relationships of the bimetallic particles spanning from the nano to the macro scale is important for the rational design of improved electrocatalysts.

In this report, we have identified the basic dealloyed morphological and compositional structures in dealloyed bimetallic nanoparticles as a function of their size. In particular, we have examined the morphology and composition of dealloyed Pt−Co and Pt−Cu nanoparticle electrocatalysts using microscopic, spectroscopic and surface sensitive techniques, such as cyclic voltammetry, high-resolution aberration-corrected high-angle annular dark field scanning transmission electron microscopy (STEM-HAADF), transmission electron microscopy (TEM), electron energy loss (EEL) spectroscopy, and energy-dispersive X-ray spectroscopy (EDS). Our results of both dealloyed Pt−Co and Pt−Cu nanoparticle catalysts indicate the existence of three different size regimes associated with characteristic structural morphologies and compositions. The three size regimes involve two different characteristic particle diameters, where features of multiple cores and pores emerge. The goal of this work is to link the observed particle structures at the nano scale to those found at the macro scale, bridging the materials gap between dealloyed nanoparticles and macroscopic highly porous bulklike bimetallic particles in corrosion science.

2. EXPERIMENTAL SECTION

2.1. Synthesis of Pt−Co and Pt−Cu alloy nanoparticles. The synthesis of Pt−Co and Pt−Cu alloy nanoparticles was conducted via liquid precursor impregnation − freeze-drying method, followed by thermal annealing in a hydrogen/argon atmosphere. All chemicals were used as received. 250 mg of 28.2 wt % Pt/HSAC (HSAC - high surface area carbon) (part no. TEC10E30E, supplied by TKK, Japan) and 316 mg of the precursor salt $Co(NO_3)_2 \cdot 6\ H_2O$ (Alfa Aesar, #010694) or 251 mg of $Cu(NO_3)_2 \cdot 2.5\ H_2O$ (Sigma Aldrich, #467855) were used for the formation of alloy nanoparticles with Pt:M (M = Co, Cu) atomic ratio of 1: 3. The precursor salt was dissolved in 3 mL of deionized water (18 MOhm at room temperature) and added to the previously already weighted amount of Pt/HSAC. The suspension was horn-ultrasonicated and subsequently freeze-dried at 0.0035 mbar for few days. Finally, the dried impregnated powder was annealed at 800 °C for 7 h in a hydrogen/argon atmosphere with a flux of 100 mL min^{-1}. The Pt−Co and Pt−Cu alloys exist mainly as substitutional disordered face-centered cubic crystal phases.[48,49,62] The resulting Pt−Co and Pt−Cu alloy nanoparticles were used for electrochemical dealloying experiments to form highly active dealloyed Pt bimetallic electrocatalysts.[48,49,62]

2.2. Electrochemical experiments. The electrochemical experiments were performed in deaerated 0.1 M $HClO_4$ electrolyte solution at room temperature using a rotating disk electrode (RDE) technique (supplied by PINE, USA) equipped with a self-made, three-compartment glass cell, a rotator (PINE, USA) and a commercial potentiostat (VSP-5, Biologic, France). The following electrodes were employed: Pt gauze as a counter electrode, mercury−mercury sulfate (MMS) electrode (Princeton Applied Research, AMETEK) as reference electrode and a rotating disk electrode (PINE, USA) with a glassy carbon (GC) disk at 5 mm diameter as working electrode. The working electrode was polished and cleaned before preparing the thin catalytic film on the GC surface.[63−65] Around 5 mg of Pt alloy catalyst powder was suspended by ultrahorn sonication in 3.98 mL of deionized water, 1.00 mL of 2-propanol and 20 μL of 5 wt % Nafion solution. Ten μL of the suspension was pipetted onto the previously polished and cleaned GC electrode and dried at 60 °C for 10 min in air. All potentials were converted and normalized with respect to the reversible hydrogen electrode (RHE) scale. Cyclic voltammograms (CVs) were recorded in a voltage range between 0.06 and 1.00 V/RHE in nitrogen-purged 0.1 M $HClO_4$ electrolyte at room temperature. The bimetallic alloy catalysts were electrochemically dealloyed to leach off cobalt or copper from the particle surface. Here, the dealloying protocol involved three voltammetric segments: three slow scans with a scan rate of 100 mV s^{-1}, 200 fast scans with 500 mV s^{-1} and finally three slow scans with 100 mV s^{-1}.

2.3. High-resolution scanning transmission electron microscopy and electron energy loss spectroscopy. The preparation of the dealloyed Pt−Co and Pt−Cu electrocatalysts for high-resolution scanning transmission electron microscopy was carried out in the following way: After the voltammetric experiments the dealloyed Pt−Co and Pt−Cu catalysts were removed completely from the GC electrode surface. The particles were subsequently immersed in a water/2-propanol solution and dispersed with a sonicator. Each sample was washed and centrifuged several times to reduce the particle agglomeration and to dissolve the residual Nafion polymer which was used in an earlier stage of the electrode preparation. Finally, the suspension was deposited on an alumina grid with holey carbon film and dried in air.

High-resolution microstructural investigations were performed in a probe-corrected FEI TITAN S 80−300 STEM equipped with a HAADF detector. The accelerating voltage of the microscope was 300 kV. 'Z-Contrast' conditions were achieved using a probe semiangle of 25 mrad and an inner collection angle of the detector of 70 mrad. EEL spectra were acquired with a Gatan image filter (GIF) Tridiem 866ERS. The energy resolution was determined from the full width at half-maximum of the zero loss peak and was about 1 eV. During the EEL line scan across the dealloyed bimetallic particles, 20 individual EEL spectra were collected and analyzed to establish the accurate chemical composition profiles.

2.4. Transmission Electron Microscopy and Energy-Dispersive X-ray Spectroscopy. A FEI TECNAI G^2 20 S-TWIN transmission electron microscope equipping a LaB_6 cathode, an energy-dispersive X-ray spectroscopy (EDS) detector and a GATAN MS794 P CCD camera was employed to investigate the particle morphology and overall chemical composition of single dealloyed Pt−Co and Pt−Cu particles above a diameter of 20 nm. The microscope operated by an accelerating voltage of 200 kV. EDS measurements were performed with a focused electron beam to establish the entire elemental composition of a single particle. The characteristic energy intensities of K- and L-line for Co/Cu and Pt were used for the quantification with the software TEM Imaging & Analysis.

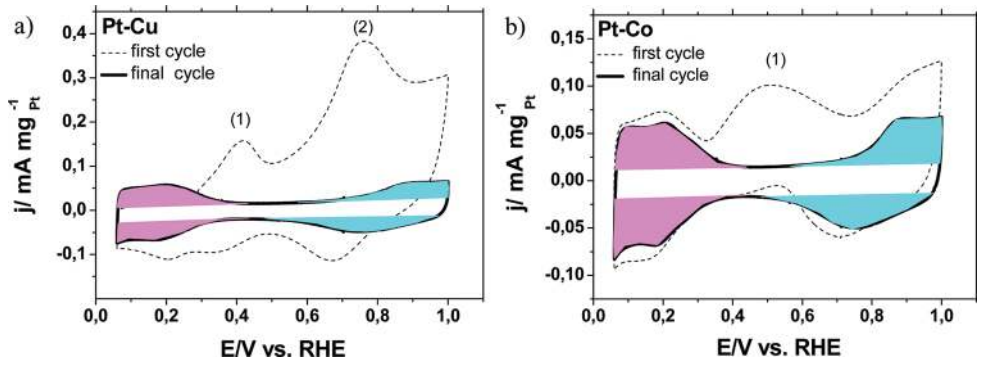

Figure 1. CV profiles of (a) Pt−Cu and (b) Pt−Co alloy nanoparticle electrocatalysts before (dashed) and after (solid line) the electrochemical dealloying process. The broad hydrogen ad-/desorption regime and redox peak couple of Pt (hydr-)oxide are indicated by red and blue areas. (a) Positions (1) and (2) signify the surface dissolution of pure bulk Cu and underpotentially deposited Cu, respectively. (b) Position (1) indicates the surface dissolution of underpotentially deposited Co.

3. RESULTS

3.1. Formation of Platinum-Enriched Particle Shell by Dealloying. Figure 1a and 1b compare the current−voltage characteristics (cyclic voltammograms, CVs) of the Pt alloy precursor electrocatalysts supported on HSAC before (dashed) and after (solid line) the electrochemical dealloying procedure. The Pt−Cu and Pt−Co exist largely as substitutional disordered cubic alloys.[48,49,62] After dealloying, both alloy catalysts exhibit the characteristic CV features of a pure platinum surface, including the broad underpotential hydrogen deposition/stripping peaks (red areas) and the irreversible peak couple indicating Pt surface oxygenates (blue areas). Strong differences are evident in the initial (dashed) CVs of the two Pt alloy precursors. Unlike Pt−Co, the Pt−Cu precursor shows no signs of anodic hydrogen stripping on the first scan, implying complete surface segregation of Cu consistent with DFT theoretical predictions.[66,67] In addition, copper dealloyed in two distinct faradic current peaks are consistent with Cu bulk dissolution (Cu−Cu bond breaking, Figure 1a, position 1) and, more anodically, with the dissolution of underpotentially deposited Cu surface atoms (Cu−Pt bond breaking, Figure 1a, position 2.[66] Due to the presence of Co on the surface of Pt alloy particles, Co atoms dissolve in a broad single voltammetric peak (1), shown in Figure 1b. Measurements of the electrocatalytic oxygen reduction (ORR) activity (see in Supporting Information) show a 3−4-fold benefit for the dealloyed Pt−Co and a 4−5-fold benefit for the dealloyed Pt−Cu nanoparticle electrocatalyst compared with the benchmark Pt nanoparticle catalyst.[43,48,49,62]

3.2. Particle Morphology and Chemical Composition before and after Dealloying. Energy-dispersive X-ray spectroscopy (EDS) revealed that the overall chemical compositions of Pt−Co and Pt−Cu catalysts changed clearly from $Pt_{37\pm2}Co_{63\pm2}$ to $Pt_{80\pm2}Co_{20\pm2}$ and from $Pt_{35\pm2}Cu_{65\pm2}$ to $Pt_{65\pm2}Cu_{35\pm2}$ after dealloying. The losses of Co and Cu are in agreement with the observed faradic dissolution peaks in the cyclic voltammetric experiments. Note, the dealloying process did not result in completely dealloyed particles. Indeed, a significant content of cobalt/copper is found inside the catalytically active nanoparticles. Furthermore, the final CV profiles for Pt−Co and Pt−Cu indicate an almost complete covering of Pt atoms on the particle surface after the dealloying process.

To establish the relationships between particle size as well as the morphological and compositional structure of individual dealloyed bimetallic particles, we used HAADF-STEM and EEL spectroscopy techniques. The image intensity of an atom column is roughly proportional to $Z^{1.6}$ for sufficiently thin objects. Platinum and cobalt/copper reveal a significant difference in the atomic number: $Z = 78$ for Pt, $Z = 27$ for Co, and $Z = 29$ for Cu which results in a distinct image contrast between Pt- and Co/Cu rich specimen regions.

Figure 2 displays HAADF overview images for Pt−Co and Pt−Cu alloy particles before and after dealloying. The well-

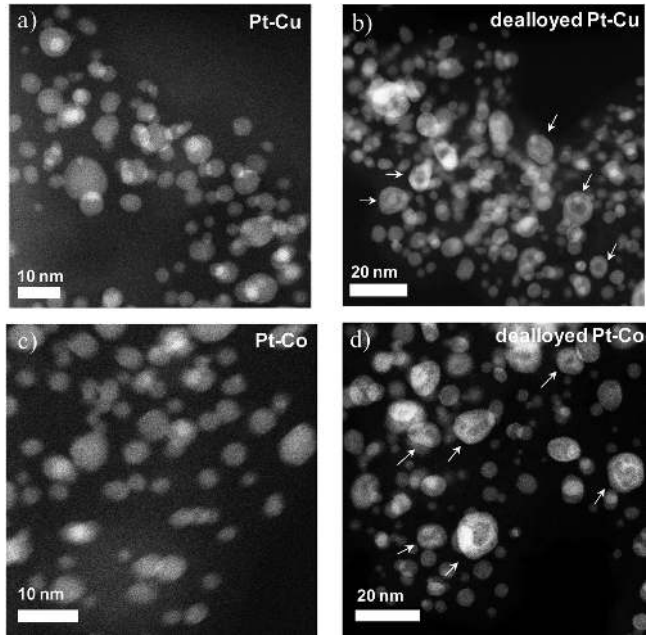

Figure 2. HAADF overview micrographs of Pt−Cu and Pt−Co particle ensembles; (a and c) before and (b and d) after dealloying. The white arrows exemplarily denote particles with nontrivial contrast features.

alloyed Pt-M precursors show a uniform contrast distribution with the highest intensity in the center of the particles. These contrast features reveal spherical shapes of the individual particles and a homogeneous chemical composition (see a and c in Figure 2). Bright contrast occurs where particles overlap along the optical axis. However, in their dealloyed structure configuration (b and d in Figure 2), the particle ensemble exhibits a variety of complex contrast patterns, indicating changes

dx.doi.org/10.1021/ja2088162 | J. Am. Chem.Soc. 2012, 134, 514−524

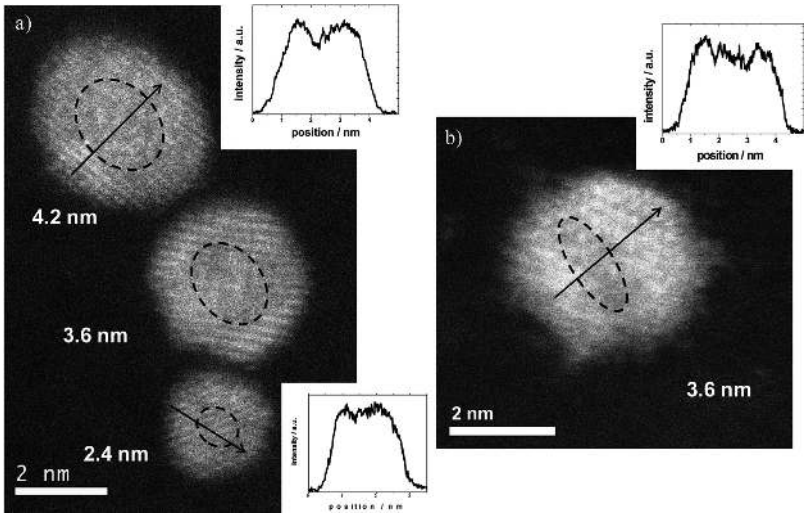

Figure 3. (a) HAADF micrograph of individual dealloyed Pt−Cu nanoparticles up to 5 nm with their according HAADF intensity line profiles. (b) HAADF micrograph of a dealloyed Pt−Co nanoparticle at 3.6 nm with the according intensity line profile. The black arrows signify the scan direction of the intensity profiles, and the dashed lines indicate the dark-shaded particle regions.

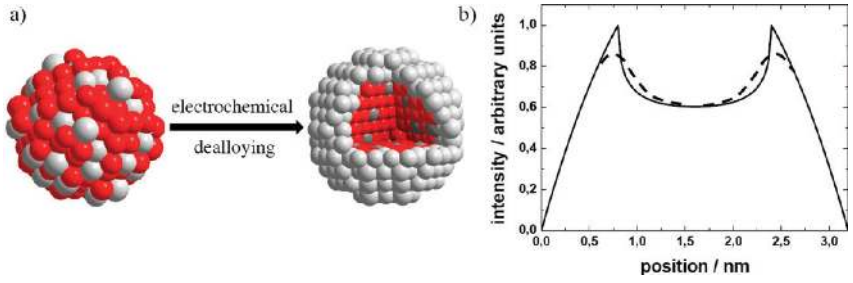

Figure 4. (a) Illustration of the formation of core−shell bimetallic nanoparticles by electrochemical dealloying. Red and light-gray spheres denote Cu atoms and Pt atoms, respectively. (b) Simulated HAADF intensity profiles of a core−shell Pt−Co nanoparticle at ∼3.5 nm with Pt shell thickness of ∼0.8 nm. Solid line in the HAADF intensity profile denotes a sharp compositional transition between the core and shell, while dashed lines indicate a smoother profile with more continuous compositional transition at the core−shell interface.

in particle morphology and intraparticle chemical composition. For instance, some selected particles with nontrivial contrast patterns are denoted by white arrows in b and d in Figure 2. Further STEM overviews of Pt−Co and Pt−Cu particles as well as selected examples are shown Figures S1 and S2 which reflect our comprehensive study (see Supporting Information [SI]).

Without more detailed analysis or comparison to calculated HAADF intensity profiles, these contrast variations may be due to the changes in thickness or composition or a combination of both. Most importantly for our discussion, however, is the question, if and how the intraparticle intensity variations are correlated with the size of the dealloyed particles; a question that has remained unaddressed to date.

3.3. Principle Nanoscale Particle Morphologies and Structures and Their Size Dependence. *3.3.1. "Single Core−Shell Nanoparticles: Dealloyed Pt−Co and Pt−Cu Nanoparticles below 5 nm Diameter.* We start with an analysis of the dealloyed particle morphologies in the smallest size regime of ≤5 nm. Figure 3 shows HAADF images for individual Pt−Co and Pt−Cu nanoparticles with a mean size of 3−4 nm. Lattice fringes are clearly resolved in each image. The dealloyed particles exhibit a spot in the center with darker shading than the outer part. This contrast feature is also reflected in the HAADF intensity line profiles (insets in Figure 3), which were taken with a line width of 0.4 nm. It shows a steep increase of the intensity at the edges of the particle, and a slight dip (upper left and right profile) or a flat plateau (lower left profile) at the center. To explain this observed course of the intensity profile, we recall that under *Z*-contrast conditions the image intensity of Pt ($Z = 78$) is much higher than that of Co ($Z = 27$) and Cu ($Z = 29$). Strictly spherical particle morphologies rule out thickness variations as a source of the central dip of the contrast patterns. Hence, the observed contrast features must be related to the variation of the chemical composition in the center of the particles, suggesting a single Co/Cu rich core and a Pt rich shell.

To corroborate our conclusion, we calculated a HAADF intensity profile of a single core−shell nanoparticle formed by dealloying of a precursor alloy particle (see Figure 4a). Figure 4b shows the calculated HAADF intensity profile for a spherical core−shell nanoparticle consisting of a ∼3.5 nm M rich alloy core and a ∼0.8 nm pure Pt shell with a sharp compositional transition between core and shell (solid line). A more continuous compositional transition between core and shell would lead to a smoother HAADF intensity profile without pronounced spikes at the core−shell interface (dashed lines). This predicted line profile is in good agreement with the experimental results and reveals a core−shell structure for this size regime. The HAADF intensity maxima of the various core−shell particles at 3−4 nm showed a mean Pt shell thickness of around 0.8 and 1.2 nm. Although the nanoparticles

dx.doi.org/10.1021/ja2088162 | J. Am. Chem.Soc. 2012, 134, 514−524

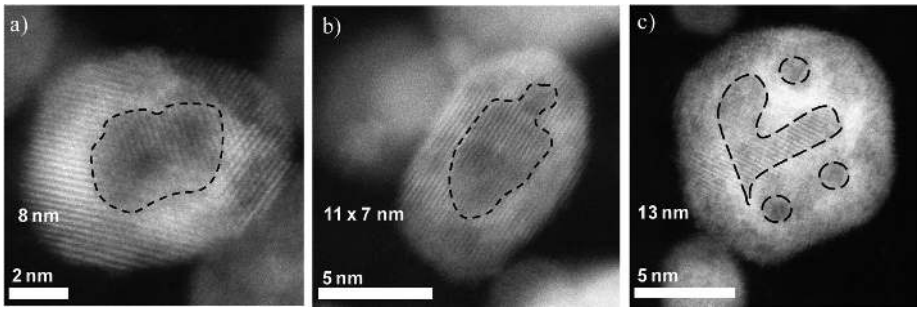

Figure 5. HAADF micrographs of individual dealloyed Pt−Co particles with various diameters of 8−15 nm. As guide to the eye, these contrast features are outlined by black dashed lines.

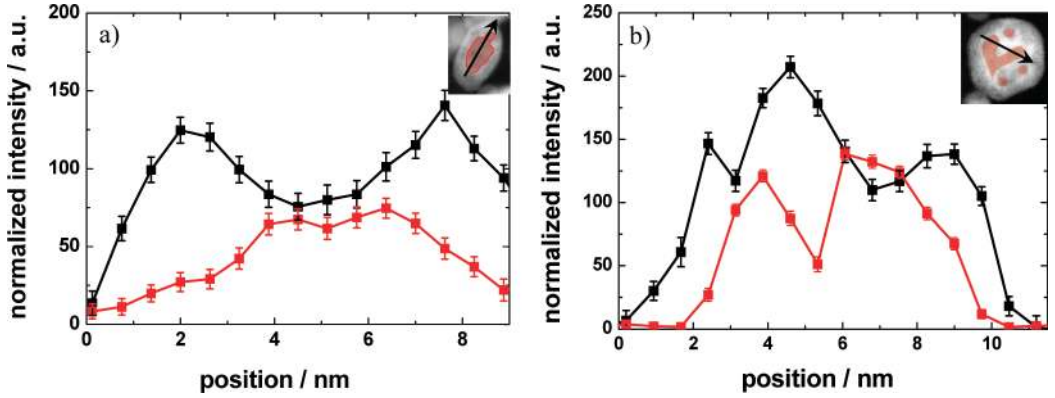

Figure 6. EEL line scan profiles for Pt (black) and Co (red) concentration in dealloyed Pt−Co nanoparticles at (a) 11 nm and (b) 13 nm. (Insert) Direction of the line scan is indicated with a black arrow, and the red area highlights the contrast features in the HAADF micrograph.

in the size regime below 5 nm appear to be basically spherical, slight deviations from an ideal centrosymmetric structure are found. Figure 3b, for example, shows a slightly elongated and off-center dark spot (dashed lines), which indicates an ellipsoidal core and a variable shell thickness around it. Nanopores or hollows were not observed in dealloyed Pt−Co and Pt−Cu nanoparticles of this size range. This is likely due to the high surface energy of voids of this size and the rapid annihilation process of vacancies by highly mobile low-coordinated Pt surface atoms, as discussed in more detail later.

3.3.2. "Multiple Cores−Shell Nanoparticles": Dealloyed Pt−Co and Pt−Cu Particles up to 20 nm Diameters. The particle morphology and intraparticle composition of dealloyed Pt−Co and Pt−Cu within the size range up to 20 nm are distinctly different from the simple core−shell structure.

Figure 5 shows a collection of HAADF micrographs for representative dealloyed Pt−Co particles between 8 and 15 nm. Lattice fringes are clearly resolved. Inside of the particles, the HAADF micrographs display contrast features which are more complex than simply dark shading in the center and bright shading in the outermost parts. As guide to the eye, these contrast features are outlined by black dashed lines in Figure 5. The frequently appearing particle motifs will now be discussed in detail considering the spectroscopic established composition profiles for Pt and Co, respectively, using EEL spectroscopy (see Figure 6). The concentration profiles of the EEL spectroscopy line scans from the Pt $M_{4,5}$ (2155−2400 eV) and Co L_3 (770−785 eV) edges are shown in black and red. The EEL signals are normalized concerning the scattering cross section of the elements. The normalized intensity can be correlated with the projected thickness of the respective element. Error bars, which were calculated according to standard deviation of the EEL data within the limit of integration in addition to the mismatch of the background fit curves, indicate a good signal-to-noise ratio of the compositional measurements.

Figure 5a shows a HAADF micrograph of a dealloyed particle at 8 nm with a dark-shaded region in the center (denoted with black dashed lines) and bright outermost edge, indicating the formation of single core−shell structure. The particle and its core, however, are not perfectly round and exhibit a slightly irregular shape. The particle seems to be broken at the upper right side.

In Figure 5b, an ellipsoidal particle with a dimension of 11 nm × 7 nm exhibits a dark-shaded, elongated core of 3 nm × 5 nm (denoted with black dashed lines). The corresponding EEL line scans for Pt and Co across this particle are shown in Figure 6a. At the upper left side, the particle is overlapped with other particles, and therefore the Co and Pt EEL signal do not drop to zero. Along the EEL scan, the Pt signal increases rapidly on the edges and reaches its maxima at 2.0 and 7.5 nm. In the center of the particle, the Pt signal shows clearly a minimum at 4.5 nm. The Co signal is almost zero at the edge and exhibits broad maxima in a range of 4 and 6.5 nm which relates to the dark-shaded, ellipsoidal core in the HAADF image (symbolized with black dashed lines in Figure 5b).

Figure 5c shows a HAADF micrograph of an almost spherical particle at 13 nm with an irregular core structure (indicated with black dashed lines). Along the EEL spectroscopy line scan shown in Figure 6b, two Co rich core regions at 4 and 6 nm are crossed which display dark contrasts in the HAADF micrograph. The Co concentration is zero below the particle surface. The Pt EEL signal exhibits three distinct maxima at 2.2, 4.5, and 8.5 nm.

dx.doi.org/10.1021/ja2088162 | J. Am. Chem.Soc. 2012, 134, 514−524

The Pt maxima agree excellently with the bright regions of the particle in the HAADF micrograph.

Our microstructural and compositional study suggests that particles in this size regime possess a complex Co rich core structure, which may even split into multiple separate core regions. Irregular shaped dark regions near the particle center directly correlated with Co rich regions (cores), while dark-shaded spots (indicated by dashed lines in Figure 5c) near the particle surface evidence Co rich regions of a few nanometers in diameter ("*Co satellite cores*").

Dealloyed Pt−Cu particles show also morphological and compositional complexation, that is very similar to the observed structure for Pt−Co particles at similar size, for instance, multiple cores with irregular shape. Figure 7 displays a representative HAADF micrograph of four, nearly spherical Pt−Cu particles with 11, 14, 15, and 22 nm diameters. Round dark regions of 5−6 nm diameter in the center are surrounded by bright outer particle shells. These contrast features indicate that copper is predominately located in the center, while platinum constitutes the outer shell. Our results suggest that Pt−Cu particles up to 15 nm diameter form a single core−shell structure, while particles with diameter greater than 20 nm show multiple irregular dark-shaded regions (Figure 7). The multiple dark-shaded regions of about 3−4 nm represent the local enrichment of copper. The Cu rich regions form multiple cores inside the particle.

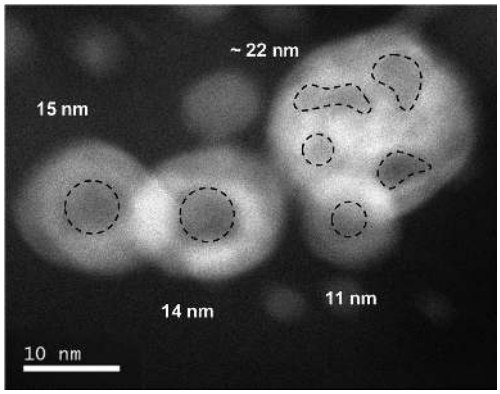

Figure 7. HAADF micrograph of individual dealloyed Pt−Cu particles in a size range of 10−22 nm. As a guide to the eye, the black dashed lines in the HAADF image indicates the dark-shaded regions.

To summarize the analysis in the size regime up to 20 nm, we have identified a characteristic particle size, referred to as $d_{\text{multiple cores}}$, of 10−15 nm that separates a single core−shell arrangement from complex multiple cores−shell structure. The characteristic particle diameter highlights a distinct morphological and compositional structure change of the dealloyed particles. Above $d_{\text{multiple cores}}$, dealloyed bimetallic particles generally exhibit dominantly multiple, less noble metal-rich cores with irregular and/or ellipsoidal shape.

3.3.3. "Nanoporous Multiple Cores−Shell Particles": Dealloyed Pt−Co and Pt−Cu Particles up to 100 nm Diameter. Figure 8a shows a representative HAADF image of an individual dealloyed Pt−Cu particle with 43 nm diameter which shows a large irregularly shaped dark region of around 20 nm in the center, bright outermost edges, and multiple dark spots close to the particle surface. In contrast to the smaller size regimes, the particle exhibits irregular dark areas directly bordering at the surface (dashed black lines in Figure 8a). Since Cu rich regions on the surface rapidly dissolve under the chosen cycling conditions, these contrast features clearly provide evidence for corrosive pits and the formation of nanopores (symbolized with white arrows in Figure 8a). The intensity variations in the dealloyed Pt−Cu particle are related to the presence of both multiple Cu rich cores and nanopores. A similar structure was also found for Pt−Cu particles in a size range of 40−70 nm. Here, Figure 8b shows a dealloyed Pt−Co particle with some surface pits (symbolized with dashed black lines).

To support our conclusion, a tilt series of HAADF micrographs was acquired which represents a three-dimensional (3D) tomographic structure picture (see short movie in SI). The tomographic study reveals a complex 3D inner structure with elongated channels like dark areas and a number of pits on its particle surface. In addition, Figure S3 (SI) shows TEM micrographs and overall chemical compositions established by EDS for various dealloyed Pt bimetallic particles in a size range between 30 and 200 nm. The EDS results of single Pt−Co particles show a final Co concentration of around 10−18 at % after dealloying, whereas the residual Cu concentration of the Pt−Cu particles is around 34 at %. These results are in excellent agreement with the overall chemical compositions of Pt−Cu and Pt−Co particle ensembles. It is noted that the Co

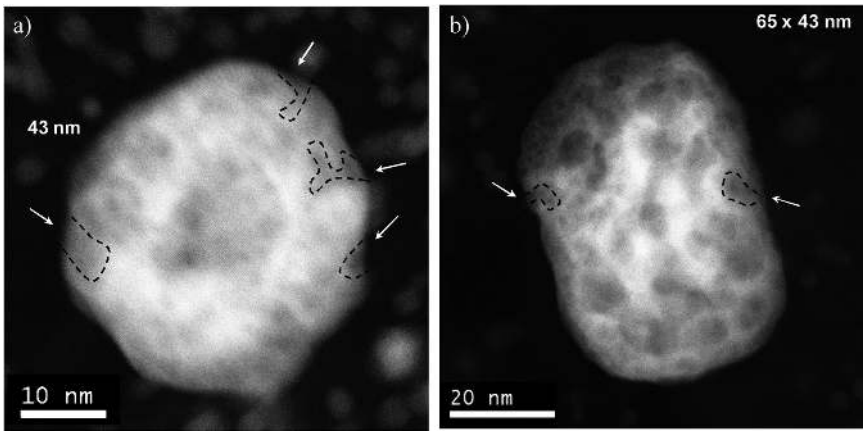

Figure 8. HAADF micrographs of dealloyed (a) Pt−Cu and (b) Pt−Co particles with diameters larger than 40 nm. As a guide to the eye, the white arrows and black dashed lines denote the surface pits (nanopores) on the particle surface.

dx.doi.org/10.1021/ja2088162 | *J. Am. Chem.Soc.* 2012, 134, 514−524

concentration loss for Pt−Co particle catalysts is higher than that for Pt−Cu due to the dissolution potentials and the oxygen adsorbate-induced surface segregation.[68,69] Nevertheless, it evidences that the large particles are not completely dealloyed after the electrochemical process.

Approaching macroscale dimensions, bulk dealloying behavior is more noticeable for particles in a size range above 100 nm. Figure 9 shows a dealloyed Pt−Cu particle at

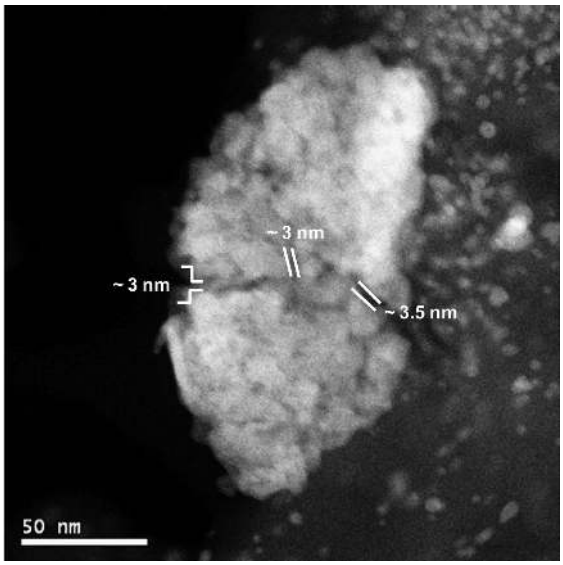

Figure 9. HAADF micrograph of dealloyed Pt−Cu particle at 100 nm × 150 nm with a clearly visible porous structure. The pores are on the order of 3 nm.

100 nm × 150 nm with clearly visible pores and ligament structure. The formed nanopores are on the order of ∼3 nm diameter and penetrate clearly the entire particle. TEM micrographs of particles at similar geometric size with the corresponding EDS results are also shown in Figure S3 (see SI). The single particles of around 100 nm still contained a Co concentration of around 17 at %, while the residual Cu concentration by comparable size was around 36 at %. Surprisingly, this value is similar to the final chemical composition of the 30−70 nm particles that show a much smaller surface-to-volume ratio. Hence, bulklike porous bimetallic particles above 100 nm diameter exhibit a much higher rate of Co/Cu loss than smaller particles under similar dealloying conditions. This is rationalized considering the much larger increase in the interfacial area of large particles during porosity evolution. Importantly, the observed size of the nanopores in the particle of Figure 9 and similar particles was about 3 nm. At particle diameters above 30−40 nm, this value appeared to be a material-characteristic value and is in excellent agreement with pore sizes of nanoporous platinum obtained by acid leaching of $Pt_{25}Cu_{75}$ alloy films at room temperature.[70,71]

To summarize our observation in the size regime of up to 100-nm size, we have uncovered the existence of a novel class of particle morphologies characterized by the presence of particles involving surfaces pits and pores of characteristic length scale coexisting with irregularly shaped multiple Co/Cu rich cores.

4. DISCUSSIONS

4.1. Size-Dependent Morphology and Chemical Composition of Dealloyed Pt−Co and Pt−Cu Particles. On the basis of our present microscopic and spectroscopic results, Figure 10 illustrates a detailed size−morphology−composition relation for dealloyed Pt−Cu and Pt−Co particle electrocatalysts in a size range of 3−100 nm. Unlike most other works, this study focuses on the dominant morphological classes of dealloyed particle electrocatalysts in their most active state. The catalysts were intentionally not treated with accelerated degradation protocols, yet were prepared and left in their dealloyed activated state.[45,48,64,72−76]

Obviously, the dealloyed Pt bimetallic particle morphology exhibits a strong size effect. The Pt shell of the dealloyed particles appears to scale with the particle size, i.e. large particles tend to exhibit a thicker Pt-enriched shell region after comparable dealloying time. This indicates that, for larger particles, the dealloying proceeds rapidly into larger depth. Our results suggest the existence of three different size−morphology regimes of dealloyed Pt−Co and Pt−Cu catalysts: With increasing size, a structural regime characterized exclusively by single core−shell structures give way to one involving multiple-core bimetallic structures. At even larger sizes, surface-pits and nanopores coexisting with multiple cores are formed. These size−morphological regimes are separated by two characteristic particle diameters, $d_{\text{multiple cores}}$ and d_{pores}.

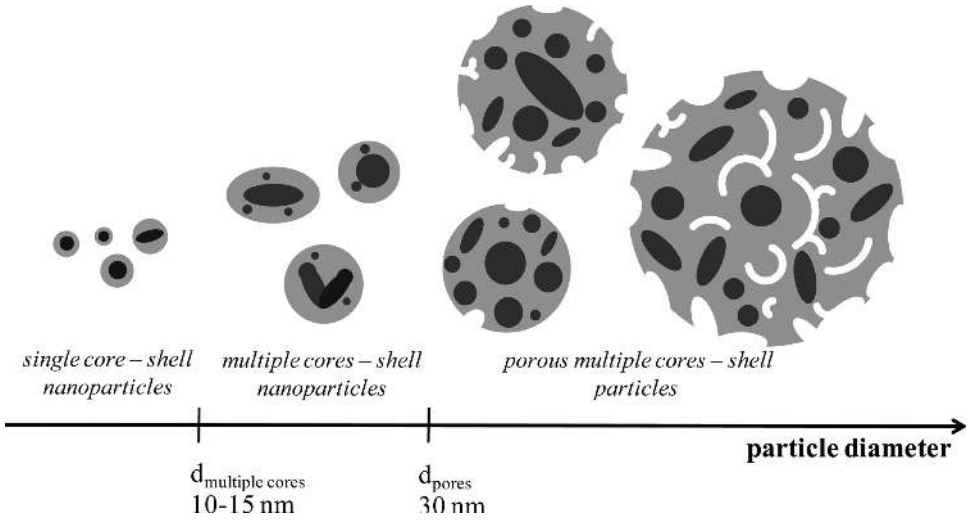

Figure 10. Illustration of the evolution in size-dependent morphology and composition of dealloyed Pt−Cu and Pt−Co particle electrocatalysts.

dx.doi.org/10.1021/ja2088162 | J. Am. Chem.Soc. 2012, 134, 514−524

The values of $d_{\text{multiple cores}}$ and d_{pores} represent the approximate lower particle size boundaries, where Cu-/Co rich multiple cores and nanopores/voids were observed to exist, respectively. They are manifestations of nanoscale effects. The kinetic and thermodynamic aspects affecting the particle structure formation as a function of particle size can be described in a consistent picture as follows:

In Pt alloys with Cu/Co content above the parting limit, Cu/Co atoms are dissolved rapidly from the particle surface by electrochemical dealloying, because the upper potential limit of 1.0 V/RHE during the applied voltage cycling is far more positive than the critical dealloying potential.[34,71] At the macro scale, dealloying of bulk binary alloys results in the evolution of porosity with a characteristic pore size. The formation of porosity is thereby controlled kinetically by the interplay of the rates of electrochemical dissolution and surface diffusion.[31,77] For instance, Pugh et al. reported that dealloying of macroscopic Pt−Cu alloys leads to characteristic 3 nm pore diameters[70,71] due to the slow surface diffusion coefficient of Pt. Due to the macroscopic size, thermodynamic interfacial energy barriers can generally be neglected. The detailed mechanisms leading up to porosity in macroscopic binary alloys were thoroughly analyzed by Erlebacher et al., who reported a detailed model for porosity evolution, highlighting the role of electrochemical dissolution and surface diffusion.[31,78]

At the nanoscale, both kinetic and thermodynamic factors significantly affect the particle structure-formation process. First, we will discuss the existence conditions for multiple Cu-/Co rich particle cores. Our data suggests that Cu-/Co rich cores are only stable above a size of 3 nm. This can be rationalized on the basis of thermodynamic interfacial energy arguments prohibiting cores with smaller diameters. To accommodate two or more of these cores, the Pt particle shell has to be at least 3 nm thick, requiring an (ideal hard sphere-based) minimum particle size to about 10 nm. This is in good agreement with our experimentally observed lower value of the characteristic particle diameter for multiple cores, $d_{\text{multiple cores}}$.

Now, we address the observed existence conditions for porosity. Voids and pores exhibit a characteristic length scale of about 3 nm, but they were, under our conditions, only observed in particles with diameters above d_{pores} = 30−40 nm. On the basis of these vastly different dimensions, thermodynamic interfacial energy arguments now fail to account for the absence of porosity, suggesting rather a largely kinetically controlled pore formation mechanism such as the Rayleigh surface instability.[77]

Rayleigh instabilities are surface diffusion-driven processes and refer to the growth of randomly formed surface pits with their high vacancy density into bulk pores and, upon channel pinching, into closed voids. Important for our discussion here is the fact that a successful Rayleigh surface instability requires the correct balance between the surface diffusivity of low-coordinated Pt atoms inside the surface pit and the Pt atoms around the pit. Pt atoms inside the pits tend to diffuse to the edges to raise their coordination. This favors the growth of the pit deeper into the particle bulk. If the surface diffusion rate of surface Pt atoms around the pit is sufficiently large, however, pits cannot grow and rather heal out, resulting in the disappearance of the initial pits. Voids then become impossible. We hypothesize that the balance between the surface diffusivities of Pt surface atoms inside pits and around pits allow for the formation of voids near the characteristic particle diameter d_{pores}, because surface atoms of large particles exhibit higher mean coordination numbers and hence lower diffusivities.

We mention in passing that recent work on void formation in particles has highlighted the role of the Kirkendall interdiffusion effect. This effect is based on bulk diffusivity differences at a bimetallic interface and involves vacancy supersaturation followed by vacancy condensation into voids on the fast diffuser side of the interface.[79−83] Examples of Kirkendall effects in nanoscale objects at elevated temperatures were reported by Henkes et al.[84] and Yin et al.[85] Considering the ambient temperatures of these studies combined with the relatively large distance a diffusing metal atom would have to overcome to reach the particle surface, we assume to exclude Kirkendall effect to explain our observations.

The two characteristic particle diameters $d_{\text{multiple cores}}$ and d_{pores} delineate three distinct size ranges with characteristic morphologies as follows:

(i) "*single core−shell nanoparticles*": single core−shell nanoparticles are exclusively formed by dealloying of particles below $d_{\text{multiple cores}}$ = 10−15 nm. The voltammetric cycling in acidic electrolyte leads to an electrochemical rapid dissolution of Co/Cu from the particle surface. This structure is characterized by a monotone drop of Co/Cu toward the particle surface. The thickness of Pt-enriched shell is around 0.8 and 1.2 nm for this size range. Due to the stronger depletion of Co by electrochemical dealloying, the Pt-enriched particle shell for Pt−Co is slightly thicker than that of Pt−Cu particles. On the basis of our earlier discussion, nanopores or hollows are not observed in the dealloyed Pt−Cu and Pt−Co catalysts of this particle size range due to thermodynamic and kinetic arguments. We emphasized that these dealloyed bimetallic nanoparticles exist in their dealloyed most active state and do not represent a stable thermodynamic final state.

(ii) "*Multiple cores−shell nanoparticles*": Nonporous particles with irregular and/or ellipsoidal shaped multiple Co/Cu rich cores are prevailing above $d_{\text{multiple cores}}$ = 10−15 nm and below d_{pores} = 30−40 nm. Our data suggest a slight metal-dependent difference in $d_{\text{multiple cores}}$ and d_{pores} between Pt−Cu and Pt−Co particles. This can be explained by the distinct dissolution potential, surface segregation, and surface diffusion behavior of Cu and Co in the presence of adsorbed oxygen species.[68,69] On the basis of our earlier discussion, fast annihilation of pit vacancies by highly mobile Pt surface atoms and decrease of surface energy suppress the formation of voids and pores. The subsurface regions with high Cu/Co concentration are undercut on the side by dealloyed regions and results in the formation of Co-/Cu rich satellite cores.

(iii) "*Porous multiple cores−shell particles*": Dealloyed bimetallic particles with diameter above d_{pores} exhibit multiple cores and various degrees of porosity ranging from surface pits to bulk nanopores and voids. Despite the decreasing surface/volume ratio, large particles reveal smaller residual composition of Co/Cu and thus a faster dealloying behavior compared to that of smaller particles. The pit formation and porosity become more and more distinct with increasing particle size presumably based on increasing surface-controlled solid-state Rayleigh instabilities.[77]

dx.doi.org/10.1021/ja2088162 | J. Am. Chem.Soc. 2012, 134, 514−524

In summary, morphology and composition of dealloyed Pt bimetallics are strongly determined by their initial particle size. We note that some of the observed size-dependent morphological and compositional structures in Pt−Cu and Pt−Co particle catalysts do not necessarily represent a stable thermodynamic final state, but rather they could be the catalytically most active, yet transient stages along a structural and compositional trajectory. However, we also emphasize that slight variations in initial alloy composition would not qualitatively alter the observed morphologies. Also values of $d_{\text{multiple cores}}$ and d_{pores} may slightly vary for different alloys.

5. CONCLUSIONS

We have uncovered how particle size affects the morphology and chemical composition of electrochemically dealloyed Pt−Co and Pt−Cu electrocatalysts. We have established in detail the size−morphology relationships of the bimetallic catalysts in their most active dealloyed state. The morphological structure and intraparticle composition of the particles correlate strongly with their size. Thereby, the interfacial energies and the size-dependent diffusion rates of Pt are playing a key controlling role. After dealloying, the overall compositions were slightly dependent on size for larger particles, where pores had emerged. This indicates a strong coupling of pore formation and rate of dealloying. On the basis of our high-resolution microscopic and spectroscopic results, we concluded the existence of three distinctly different size−morphology regimes of dealloyed active Pt−Co and Pt−Cu catalysts,

- "*single core−shell nanoparticle*": The single core−shell structure is exclusively formed by dealloying up to a characteristic particle size ($d_{\text{multiple cores}}$ = 10−15 nm).
- "*multiple cores−shell nanoparticles*": Multiple Co-/Cu rich cores with irregular and/or ellipsoid shape become prevalent in nonporous dealloyed particles above this characteristic particle diameter $d_{\text{multiple cores}}$. The formation of multiple cores is caused by the thermodynamic interfacial energy arguments and the inhomogeneous distribution of diffusing Pt surface atoms, where subsurface regions with high Cu/Co concentration are protected against further dealloying.
- Pores and voids of a material-characteristic length scale of roughly 3 nm observed in Pt binary alloys at the macro scale cannot be formed at particles below 20 nm due to the thermodynamic and kinetical aspects.
- "*porous multiple cores−shell particles*": With increasing particle size the formation of pores becomes prevalent. Above the characteristic particle diameter of 30 nm, Pt−Co and Pt−Cu clearly exhibit surface pits (nanopores) and multiple cores inside the particles. Surface pores indicate the degree of porosity after dealloying. Above 100 nm, the macroscopic bulklike particles show a significant Co/Cu concentration and nanporous structures on the order of 3 nm pore diameter after dealloying. Despite the decreasing surface/volume ratio with increasing particle size, the large particles are leached off stronger and therefore form increased pores and ligaments structures. The formation of porosity is thereby controlled kinetically by the interplay of the rates of electrochemical dissolution and surface diffusion.
- Our results link morphological insight into dealloyed Pt−Co and Pt−Cu particles at the nanoscale to macroscopic corrosion phenomena, filling the material gap between core−shell nanoparticles and highly porous bulklike particles. The identified size−morphology−composition relationships are likely to be of general importance in understanding the dealloying of other Pt bimetallics.

■ ASSOCIATED CONTENT

Supporting Information

Table S1: Pt mass based and Pt surface area specific activities of dealloyed Pt−Co and Pt−Cu electrocatalysts for the oxygen reduction reaction compared with benchmark 28.2 wt % Pt/HSAC catalyst; Figure S1: Collocation of high-resolution HAADF micrographs of dealloyed Pt−Co particles grouped by size; Figure S2: Collocation of high-resolution HAADF micrographs of dealloyed Pt−Cu particles grouped by size; Figure S3: TEM images and EDS measurements of single dealloyed Pt−Cu and Pt−Co particles larger than 30 nm diameter after dealloying; movie of the three-dimensional tomographic structure picture of a dealloyed Pt−Co particle, shown in Figure 8b. This material is available free of charge via the Internet at http://pubs.acs.org.

■ AUTHOR INFORMATION

Corresponding Author

mehtap.oezaslan@tu-berlin.de

■ ACKNOWLEDGMENTS

We thank Dr. Lothar Houben, Dipl.-Chem. Frédéric Hasché and Annette Wittebrock for support and contributions. We thank Dipl.-Ing. (FH) Ulrich Gernert and Dipl.-Ing. (FH) Sören Selve for the possibility of using TEM and EDS techniques at Zentraleinrichtung für Elektronenmikroskopie of Technische Universität Berlin. This project was supported by the Technische Universität Berlin and Ernst Ruska Center, Jülich, Germany. P.S. acknowledgement funding by the Cluster of Excellence in Catalysis (UNICAT) funded by the DFG and managed by the TU Berlin.

■ REFERENCES

(1) Sinfelt, J. H. *Bimetallic Catalysts: Discoveries, Concepts, and Applications*; John Wiley & Sons: London, 1983.
(2) Ross, P. N. In *Electrocatalysis*; Lipkowski, J., Ross, P. N., Eds.; Wiley: New York, 1998, pp 43−74.
(3) Markovic, N. M.; Schmidt, T. J.; Stamenkovic, V.; Ross, P. N. *Fuel Cells* **2001**, *1*, 105.
(4) Stamenkovic, V.; Grgur, B. N.; Ross, P. N.; Markovic, N. M. *J. Electrochem. Soc.* **2005**, *152*, A277−A282.
(5) Rodriguez, J. A.; Goodman, D. W. *Science* **1992**, *257*, 897−903.
(6) Schuette, W. L.; Schweizer, A. E. *Stud. Surf. Sci. Catal.* **2001**, *134*, 263−278.
(7) Mukerjee, S.; Urian, R. C. *Electrochim. Acta* **2002**, *47*, 3219−3231.
(8) Roth, C.; Papworth, A. J.; Hussain, I.; Nichols, R. J.; Schiffrin, D. J. *J. Electroanal. Chem.* **2005**, *581*, 79−85.
(9) Azzam, K. G.; Babich, I. V.; Seshan, K.; Leffert, L. *J. Catal.* **2007**, *251*, 163−171.
(10) Wang, C.; Chi, M.; Wang, G.; Vliet, D. v. d.; Li, D.; More, K.; Wang, H.-H.; Schlueter, J. A.; Markovic, Nenad M.; Stamenkovic, V. R. *Adv. Funct. Mater.* **2011**, *21*, 147.
(11) Wang, C.; van der Vliet, D.; More, K. L.; Zaluzec, N. J.; Peng, S.; Sun, S.; Daimon, H.; Wang, G.; Greeley, J.; Pearson, J.; Paulikas, A. P.; Karapetrov, G.; Strmcnik, D.; Markovic, N. M.; Stamenkovic, V. R. *Nano Lett.* **2011**, *11*, 919−926.
(12) Mani, P.; Srivastava, S.; Strasser, P. J. *Phys. Chem. C* **2008**, *112*, 2770−2778.
(13) Strasser, P.; Oezaslan, M.; Hasché, F.; Koh, S.; Yu, C.; Srivastava, R. *Chem.-Ing.-Tech.* **2008**, *80*, 1267.

(14) Sao-Joao, S.; Giorgio, S.; Penisson, J. M.; Chapon, C.; Bourgeois, S.; Henry, C. *J. Phys. Chem. B* **2005**, *109*, 342−347.
(15) Soal, N. S.; Ebels, U.; Mohwald, H.; Giersig, M. *J. Phys. Chem. B* **2003**, *107*, 7351−7454.
(16) Giorgio, S.; Henry, C. R. *Eur. Phys. J. Appl. Phys.* **2002**, *20*, 23−27.
(17) Zhang, J.; Lima, F. H. B.; Shao, M. H.; Sasaki, K.; Wang, J. X.; Hanson, J.; Adzic, R. R. *J. Phys. Chem. B* **2005**, *109*, 22701−22704.
(18) Hasché, F.; Oezaslan, M.; Strasser, P. *J. Electrochem. Soc.* **2012**, *159* (1), B25−B34.
(19) Wang, J. X.; Inada, H.; Wu, L.; Zhu, Y.; Choi, Y. M.; Liu, P.; Zhou, W.-P.; Adzic, R. R. *J. Am. Chem. Soc.* **2009**, *131*, 17298−17302.
(20) Wang, J. X.; Ma, C.; Choi, Y.; Su, D.; Zhu, Y.; Liu, P.; Si, R.; Vukmirovic, M. B.; Zhang, Y.; Adzic, R. R. *J. Am. Chem. Soc.* **2011**, *133*, 13551−13557.
(21) Strasser, P.; Koh, S.; Anniyev, T.; Greeley, J.; More, K.; Yu, C.; Liu, Z.; Kaya, S.; Nordlund, D.; Ogasawara, H.; Toney, M. F.; Nilsson, A. *Nature Chem.* **2010**, *2*, 454−460.
(22) Adzic, R. R.; Zhang, J.; Sasaki, K.; Vukmirovic, M. B.; Shao, M.; Wang, J. X.; Nilekar, A. U.; Mavrikakis, M.; Valerio, J. A.; Uribe, F. *Top. Catal.* **2007**, *46*, 249−262.
(23) Stamenkovic, V. R.; Fowler, B.; Mun, B. S.; Wang, G.; Ross, P. N.; Lucas, C. A.; Markovic, N. M. *Science* **2007**, *315*, 493.
(24) Stamenkovic, V.; Mun, B. S.; Arenz, M.; Mayerhofer, K. J. J.; Lucas, C. A.; Wang, G.; Ross, P. N.; Markovic, N. *Nat. Mater.* **2007**, *6*, 241.
(25) Yang, R.; Leisch, J.; Strasser, P.; Toney, M. F. *Chem. Mater.* **2010**, *22*, 4712−4720.
(26) Yang, R.; Strasser, P.; Toney, M. F. *J. Phys. Chem. C* **2011**, *115*, 9074−9080.
(27) Hunt, L. B. *Gold Bull.* **1976**, *9*, 134−139.
(28) Lechtman, H. *Sci. Am.* **1984**, *250*, 56−63154.
(29) Raney, M. U.S. Pat. No. 1,628,190, 1927
(30) Snyder, J.; Fujita, T.; Chen, M. W.; Erlebacher, J. *Nat. Mater.* **2010**, *9*, 904−907.
(31) Erlebacher, J.; Aziz, M. J.; Karma, A.; Dimitrov, N.; Sieradzki, K. *Nature* **2001**, *410*, 450−453.
(32) Newman, R. C.; Sieradzki, K. *Science* **1994**, *263*, 1708−1709.
(33) Corcoran, S. G. In *Critical Factors in Localized Corrosion III*; Kelley, R. G., Frankel, G. S., Natishan, P. M., Newman, R. C., Eds.; Electrochemical Society: Pennington, NJ, 2000; Vol. *98-17*, p 500−507.
(34) Rugolo, J.; Erlebacher, J.; Sieradzki, K. *Nat. Mater.* **2006**, *5*, 946−949.
(35) Renner, F. U.; Stierle, A.; Dosch, H.; Kolb, D. M.; Lee, T. L.; Zegenhagen, J. *Nature* **2006**, *439*, 707−710.
(36) Renner, F. U.; Stierle, A.; Dosch, H.; Kolb, D. M.; Lee, T. L.; Zegenhagen, J. *Phys. Rev. B* **2008**, *77*, 235433.
(37) Renner, F. U.; Stierle, A.; Dosch, H.; Kolb, D. M.; Zegenhagen, J. *Electrochem. Commun.* **2007**, *9*, 1639.
(38) Dursun, A.; Pugh, D. V.; Corcoran, A. G. *J. Electrochem. Soc.* **2005**, *152*, B65−B72.
(39) Aziz, D.; Dylan, V. P.; Sean, G. C. *Electrochem. Solid-State Lett.* **2003**, *6*, B32−B34.
(40) Pareek, A.; Borodin, S.; Bashir, A.; Ankah, G. N.; Keil, P.; Eckstein, G. A.; Rohwerder, M.; Stratmann, M.; Gründer, Y.; Renner, F. U. *J. Am. Chem. Soc.* **2011**, *133*, 18264−18271.
(41) Strasser, P. In *Handbook of Fuel Cells:Advances in Electrocatalysis, Materials, Diagnostics and Durability*; Vielstich, W., Gasteiger, H. A., Yokokawa, H., Eds.; John Wiley & Sons Ltd.: Chichester, West Sussex, UK, 2009; Vols. *5, 6*, pp 30−47.
(42) Strasser, P. *Rev. Chem. Eng.* **2009**, *25*, 255−295.
(43) Oezaslan, M.; Hasché, F.; Strasser, P. *ECS Trans.* **2010**, *33*, 333−341.
(44) Hasché, F.; Oezaslan, M.; Strasser, P. *Phys. Chem. Chem. Phys.* **2010**, *12*, 15251−15258.
(45) Koh, S.; Strasser, P. *J. Am. Chem. Soc.* **2007**, *129*, 12624−12625.
(46) Srivastava, R.; Mani, P.; Hahn, N.; Strasser, P. *Angew. Chem., Int. Ed* **2007**, *46*, 8988−8991.
(47) Mani, P.; Srivastava, R.; Strasser, P. *J. Power Sources* **2011**, *196*, 666−673.
(48) Oezaslan, M.; Strasser, P. *J. Power Sources* **2011**, *196*, 5240−5249.
(49) Oezaslan, M.; Hasché, F.; Strasser, P. *Chem. Mater.* **2011**, *23*, 2159−2165.
(50) Koh, S.; Strasser, P. *J. Electrochem. Soc.* **2010**, *157*, B585−B591.
(51) Gasteiger, H. A.; Markovic, N. M. *Science* **2009**, *324*, 48−49.
(52) Holby, E. F.; Sheng, W.; Shao-Horn, Y.; Morgan, D. *Energy Environ. Sci.* **2009**, *2*, 865−871.
(53) Shao-Horn, Y.; Sheng, W.; Chen, S.; Ferreira, P.; Holby, E.; Morgan, D. *Top. Catal.* **2007**, *46*, 285−305.
(54) Chen, S.; Sheng, W.; Yabuuchi, N.; Ferreira, P. J.; Allard, L. F.; Shao-Horn, Y. *J. Phys. Chem. C* **2009**, *113*, 1109−1125.
(55) Chen, S.; Ferreira, P. J.; Sheng, W.; Yabuuchi, N.; Allard, L. F.; Shao-Horn, Y. *J. Am. Chem. Soc.* **2008**, *130*, 13818−13819.
(56) Sasaki, K.; Naohara, H.; Cai, Y.; Choi, Y. M.; Liu, P.; Vukmirovic, M. B.; Wang, J. X.; Adzic, R. R. *Angew. Chem., Int. Ed.* **2010**, *49*, 8602−8607.
(57) Wang, C.; Chi, M.; Li, D.; Strmcnik, D.; van der Vliet, D.; Wang, G.; Komanicky, V.; Chang, K.-C.; Paulikas, A. P.; Tripkovic, D.; Pearson, J.; More, K. L.; Markovic, N. M.; Stamenkovic, V. R. *J. Am. Chem. Soc.* **2011**, *133*, 14396−14403.
(58) Dubau, L.; Durst, J.; Maillard, F.; Guétaz, L.; Chatenet, M.; André, J.; Rossinot, E. *Electrochim. Acta* **2011**, *56*, 10658−10667.
(59) Maillard, F.; Dubau, L.; Durst, J.; Chatenet, M.; André, J.; Rossinot, E. *Electrochem. Commun.* **2010**, *12*, 1161−1164.
(60) Wang, J. X.; Ma, C.; Choi, Y.; Su, D.; Zhu, Y.; Liu, P.; Si, R.; Vukmirovic, M. B.; Zhang, Y.; Adzic, R. R. *J. Am. Chem. Soc.* **2011**, *133*, 13551−13557.
(61) Chen, S.; Gasteiger, H. A.; Hayakawa, K.; Tada, T.; Shao-Horn, Y. *J. Electrochem. Soc.* **2010**, *157*, A82−A97.
(62) Hasché, F.; Oezaslan, M.; Strasser, P. *ChemCatChem* **2011**, *3*, 1805−1813.
(63) Strasser, P.; Stemwedel, J.; Ross, J. *J. Phys. Chem.* **1993**, *97*, 2851−2862.
(64) Liu, Z.; Yu, C.; Rusakova, I.; Huang, D.; Strasser, P. *Top. Catal.* **2008**, *49*, 241−250.
(65) Fechner, F.; Strasser, P.; Eiswirth, M.; Schneider, F. W.; Munster, A. F. *Chem. Phys. Lett.* **1999**, *313*, 205−210.
(66) Strasser, P.; Koh, S.; Greeley, J. *Phys. Chem. Chem. Phys.* **2008**, *10*, 3670−3683.
(67) Hammer, B.; Norskov, J. K. In *Advances in Catalysis*; Academic Press: New York, 2000; Vol. *45*, pp 71−129.
(68) Mayrhofer, K. J. J.; Juhart, V.; Hartl, K.; Hanzlik, M.; Arenz, M. *Angew. Chem., Int. Ed.* **2009**, *48*, 3529−3531.
(69) Mayrhofer, K. J. J.; Hartl, K.; Juhart, V.; Arenz, M. *J. Am. Chem. Soc.* **2009**, *131*, 16348−16349.
(70) Pugh, D. V.; Dursun, A.; Corcoran, S. G. *J. Mater. Res.* **2003**, *18*, 216.
(71) Pugh, D. V.; Dursun, A.; Corcoran, S. G. *J. Electrochem. Soc.* **2005**, *152*, B455−B459.
(72) Koh, S.; Hahn, N.; Yu, C.; Strasser, P. *J. Electrochem. Soc.* **2008**, *155*, B1281−1288.
(73) Koh, S.; Leisch, J.; Toney, M. F.; Strasser, P. *J. Phys. Chem. C* **2007**, *111*, 3744−3752.
(74) Liu, Z.; Koh, S.; Yu, C.; Strasser, P. *J. Electrochem. Soc.* **2007**, *154*, B1192−B1199.
(75) Srivastava, R.; Mani, P.; Strasser, P. *J. Power Sources* **2009**, *190*, 40−47.
(76) Neyerlin, K. C.; Srivastava, R.; Yu, C.; Strasser, P. *J. Power Sources* **2009**, *186*, 261−267.
(77) Erlebacher, J. *Phys. Rev. Lett.* **2011**, *106*, 225504.
(78) Erlebacher, J.; Seshadri, R. *MRS Bull.* **2009**, *34*, 561−568.
(79) Yin, Y.; Rioux, R. M.; Erdonmez, C. K.; Hughes, S.; Somorjai, G. A.; Alivisatos, A. P. *Science* **2004**, *304*, 711−714.
(80) Huang, H. C. W. *Appl. Phys. Lett.* **1982**, *41*, 724−726.
(81) Glodán, G.; Cserháti, C.; Beszeda, I.; L. Beke, D. *Appl. Phys. Lett.* **2010**, *97*, 113109.

(82) Fan, H. J.; Gösele, U.; Zacharias, M. *Small* **2007**, *3*, 1660−1671.
(83) Aldinger, F. *Acta Metall.* **1974**, *22*, 923−928.
(84) Henkes, A. E.; Vasquez, Y.; Schaak, R. E. *J. Am. Chem. Soc.* **2007**, *129*, 1896−1897.
(85) Yin, Y.; Erdonmez, C. K.; Cabot, A.; Hughes, S.; Alivisatos, A. P. *Adv. Funct. Mater.* **2006**, *16*, 1389−1399.